A statistical analysis of the distribution of cordierite and biotite in hornfels from the Bugaboo contact aureole: implications for the kinetics of porphyroblast crystallization

A. PETLEY-RAGAN,[1] F. GAIDIES[1] AND D.R.M. PATTISON[2]

[1]Department of Earth Sciences, Carleton University, Ottawa K1S 5B6, Canada (ariannepetleyragan@cmail.carleton.ca)
[2]Department of Geoscience, University of Calgary, Calgary T2N 1N4, Canada

ABSTRACT   The three-dimensional disposition of cordierite and biotite crystals in a hornfels from the contact aureole of the Bugaboo Batholith is quantified using high-resolution X-ray micro-computed tomography and global as well as scale-dependent pattern statistics. The results demonstrate a random distribution of cordierite and biotite crystal sizes for all scales across the entire rock volume studied indicative of interface-controlled prograde metamorphic reaction kinetics. The reaction considered responsible for the mineral assemblage and the formation of cordierite and biotite in the hornfels is $Ms + Chl + Qtz = Crd + And + Bt + H_2O$. Rock-specific phase equilibria point to metamorphic conditions of ~ 520–$550\,°C$ and 3 kbar for this reaction. The common approach to approximate the shape of crystals as spherical underestimates the influence of the Strauss hard-core process on rock texture and may be misinterpreted to reflect ordering of crystal sizes by inhibition of nucleation and growth commonly associated with diffusion-controlled reaction kinetics. According to our findings, Strauss hard-core ordering develops at length scales equal to and less than the average major axis of the crystal population. This is significantly larger than what is obtained if a spherical crystal geometry would be assumed, and increases with deviation from sphericity. For the cordierite and biotite populations investigated in this research, Strauss hard-core ordering developed at length scales of up to ~ 2.2 and 1.25 mm, respectively, which is almost 1 mm longer than the scales that would be obtained if a spherical geometry would have been assumed. Our results highlight the importance of a critical assessment of the geometrical model assumptions commonly applied in the three-dimensional analysis of crystal size distributions, and underline the need for a quantitative understanding of interface processes in order to appreciate their role in the kinetics of contact metamorphic reactions and rock texture formation.

Key words: interface-controlled nucleation and growth; non-spherical crystals; Strauss hard-core ordering; XR-CT.

INTRODUCTION

The size, abundance, shape and spatial distribution of metamorphic minerals bears important information on the rates and mechanisms of fundamental processes that take place during metamorphic crystallization (e.g. Kretz, 1974; Fisher, 1978; Carlson, 1989). X-ray computed tomography (XR-CT) has become the method of choice to study the three-dimensional (3D) distribution of minerals in rocks (e.g. Ketcham & Carlson, 2001) as it allows investigation of relatively large sample volumes at sufficiently high resolution required for statistically meaningful analyses, and as its non-destructive fashion permits further studies such as mineral chemical, isotopic or crystallographic analyses of select grains identified through XR-CT (e.g. Chernoff & Carlson, 1997 1999; Robyr *et al.*, 2009; Gaidies *et al.*, 2011, 2015). Metapelitic garnet is commonly chosen as the prime

mineral for metamorphic texture analysis (e.g. Denison *et al.*, 1997; Daniel & Spear, 1999; Hirsch *et al.*, 2000; Ketcham *et al.*, 2005; Hirsch & Carlson, 2006; Hirsch, 2008; Gaidies *et al.*, 2015), given its key importance for the determination of metamorphic pressure–temperature–time $(P-T-t)$ trajectories (e.g. Spear, 1993), and as its specific attenuation properties allow it to be easily detected by XR-CT (Denison *et al.*, 1997). Other metamorphic minerals investigated texturally using XR-CT include biotite (Hirsch & Carlson, 2006), periclase (Müller *et al.*, 2009) and andalusite (Sayab *et al.*, 2015).

This study presents quantitative information on the distribution of cordierite formed in metapelites during contact metamorphism associated with the emplacement of the Bugaboo Batholith in southeastern British Columbia (Pattison & DeBuhr, 2015). To the knowledge of the authors, this is the first quantitative textural analysis of cordierite. As cordierite has

X-ray attenuation properties similar to those of many matrix phases in metapelitic rocks, automatic identification and segmentation of this mineral in CT data sets is currently not possible. For this reason, an alternative approach has been developed to statistically quantify the 3D distribution of cordierite in XR-CT data. In addition, the distribution of biotite in the same rock has been investigated through XR-CT and the deviation of cordierite and biotite crystal shape from spherical geometry, and its implications for the interpretation of common statistical correlation functions are discussed. The textural analysis is integrated with petrographic and mineral chemical data, and information obtained from phase equilibria modelling providing new insight into the nucleation and growth mechanisms of cordierite and biotite during contact metamorphism.

BUGABOO GEOLOGY

The Bugaboo Batholith is a mid-Cretaceous intrusion (*c.* 107 ± 5 Ma, Brandon & Lambert, 1992) located in the Purcell Mountains of southeastern British Columbia (Fig. 1a). It was emplaced in regionally deformed and metamorphosed Neoproterozoic turbiditic strata of the Horsethief Creek Group, resulting in a contact aureole of ∼1 km width. That part of the Horsethief Creek Group that was not affected by contact metamorphism associated with the intrusions of the granitoid bodies contains mineral assemblages characteristic of the Barrovian chlorite zone.

Figure 1b illustrates the distribution of metamorphic rocks in the Cobalt Lake area of the Bugaboo aureole, based on the petrographic analysis conducted by Pattison & DeBuhr (2015). The majority of the hornfelses in this area contain porphyroblasts of biotite, andalusite and cordierite in a weakly foliated matrix of white mica, plagioclase, ilmenite and quartz. On the basis of phase equilibria modelling performed on representative rock samples from the aureole, Pattison & DeBuhr (2015) estimate a contact metamorphic pressure of ∼3.0 kbar for this area.

Zone 1 of the aureole extends from the first appearance of andalusite and cordierite to the disappearance of primary chlorite. The outer-most part of this zone, referred to as Zone 1a (Fig. 1b), contains rocks composed of chlorite and various combinations of neoblasts of andalusite, plagioclase and patchy aggregates of relatively coarse-grained chlorite and white mica interpreted to reflect the complete pseudomorphic replacement of cordierite (Pattison & DeBuhr, 2015). With a few scattered exceptions in Zone 1a, the first occurrence of biotite marks the transition to Zone 1b and coincides with an increase in cordierite and andalusite abundance. Across the narrow width (∼50 m) of Zone 1b, the abundance of chlorite decreases, whereas cordierite, andalusite and biotite modal abundances increase (fig. 8 of Pattison & DeBuhr, 2015).

The transition from Zone 1 to Zone 2 is marked by the disappearance of primary chlorite and the presence of biotite, andalusite and cordierite. Zone 2 is the widest zone of the aureole (Fig. 1b) and comprises rocks with porphyroblast textures that transition from post- to pre-kinematic relative to the latest deformation of the matrix, most likely reflecting increasing degrees of emplacement-related stress as the contact is approached. At the highest grade, closest to the contact with the batholith, rocks of Zone 2 may additionally contain sparse fibrolitic sillimanite, defining a narrow (∼40 m) Zone 2b (Fig. 1b).

The presence of K-feldspar marks entry into Zone 3. At their lowest grade, rocks from this zone south of Cobalt Lake (Fig. 1b) contain both K-feldspar and primary white mica. This assemblage is characteristic of Zone 3a. The absence of primary white mica defines rocks of Zone 3b. Close to the contact, in an area north of Cobalt Lake, migmatitic rocks are locally developed (Fig. 1b) and are observed to contain leucosomes with quartz, feldspar and biotite
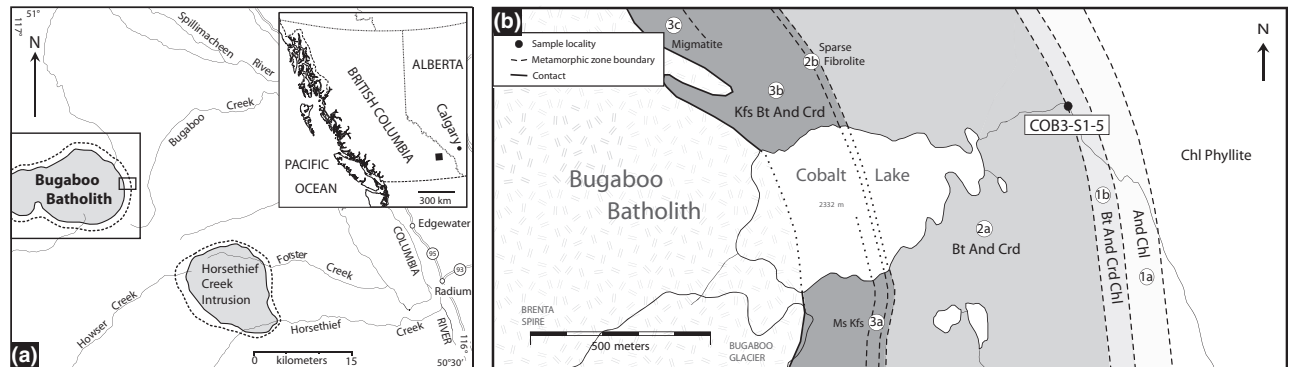

Fig. 1. (a) Location of the Purcell Mountains in southeastern British Columbia, Canada. The Bugaboo Batholith is part of a suite of granitoid intrusions in the Purcell Mountains. Cobalt Lake is located along the eastern margin of the batholith. (b) Geological map of the contact aureole and its metamorphic zones at Cobalt Lake based on Pattison & DeBuhr (2015) with the location of COB3-S1-5. Figures edited after DeBuhr (1999) and Pattison & DeBuhr (2015), and mineral abbreviations after Kretz (1983).

(Pattison & DeBuhr, 2015). Those rocks are part of Zone 3c. Fibrolite is observed throughout Zone 3, but is present only as a minor phase.

The sample investigated in this study is representative of the highest grade rocks of Zone 1b (COB3-S1-5 in Fig. 1b). The mode of this sample is given in fig. 8 and table S2 of Pattison & DeBuhr (2015) and the bulk rock composition is given in Table 1 (see also table S4 and appendix S2 of Pattison & DeBuhr, 2015). Using modal, textural and mineral chemical constraints, Pattison & DeBuhr (2015) inferred that the contact metamorphic reaction that produced the mineral assemblage of COB3-S1-5, and of the other metapelites of Zone 1b, was (mineral abbreviations after Kretz, 1983)

$$Ms + Chl + Qtz = Crd + And + Bt + H_2O. \quad (1)$$
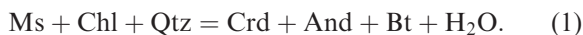
The specific X-ray attenuation properties of the minerals in sample COB3-S1-5 allow the statistical textural analysis of the cordierite and biotite content (Fig. 2). Representative rock samples from other zones of the aureole were also investigated by XR-CT but the low attenuation contrasts of their cordierite populations did not permit a statistically meaningful textural analysis.

METHODS

Phase equilibria modelling

In their study of the Bugaboo aureole, Pattison & DeBuhr (2015) attempted to reproduce the modal, textural and chemical features of the pelitic hornfelses using different thermodynamic data sets and activity–composition relations. In this study, the bulk rock composition of COB3-S1-5 (Table 1) is used to calculate the phase relations specific to this sample using the same thermodynamic data sets used in Pattison & DeBuhr (2015). In order to test the possible effects of variations in fluid composition on equilibrium phase relations, the metamorphic fluid is modelled both as a pure H_2O-fluid and a carbon, oxygen, and hydrogen-bearing (COH) phase produced by the equilibration of H_2O and excess graphite according to Connolly & Cesare (1993) following the method of Evans & Powell (2006) and Evans *et al.* (2010).
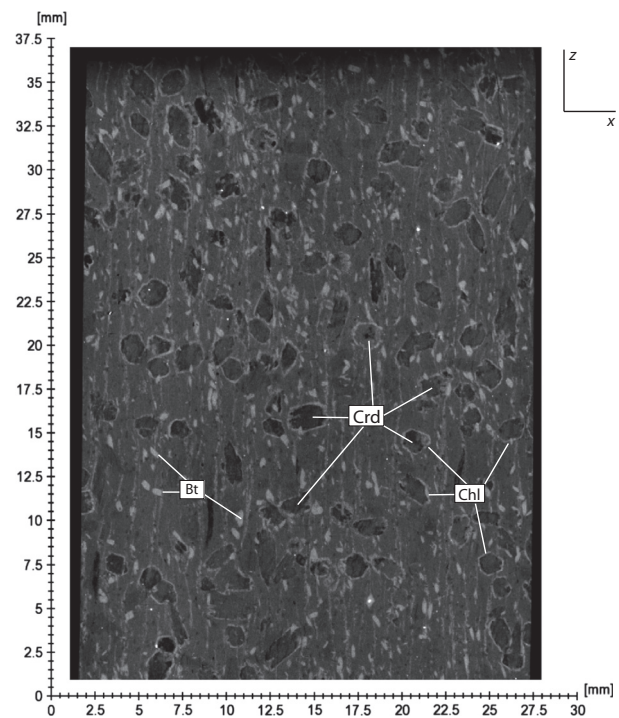

Fig. 2. Example of a greyscale image of the CT data of COB3-S1-5 produced by SkyScan software. Biotite (Bt) and chlorite (Chl) are characterized by relatively high X-ray attenuation whereas cordierite (Crd) is a lower attenuating phase similar to the fine-grained rock matrix which is predominantly composed of white mica, plagioclase and quartz. Andalusite is not visible in the CT data (see Discussion).

Electron probe micro-analysis

A Cameca Camebax MBX electron probe micro-analyser (EPMA) at Carleton University was used to study the chemistry of minerals in COB3-S1-5 and to identify any chemical zoning present in porphyroblasts. All mineral spot analyses were acquired under a beam current of 20 nA and an accelerating voltage of 20 kV. In order to achieve 40,000 counts for each element, the spots were analysed for 15–30 s. Profiles across the most inclusion-free and unaltered cordierites consisted of spots spaced at 20 μm intervals; however, due to their poikiloblastic nature an inclusion-free spot was manually chosen every 100 μm to obtain a minimum number of accurate analyses for each grain. The Cameca PAP procedure was applied to correct for matrix effects.

X-ray micro-computed tomography

In order to obtain the size, shape, abundance and spatial distribution of biotite and cordierite in the rock sample, a 3.6 cm long cylindrical core with a diameter of ~2.5 cm was scanned using a SkyScan 1173 high resolution X-ray micro-computed tomography

Table 1. Bulk rock composition of COB3-S1-5 based on XRF analysis (table S4 and appendix S1 of Pattison & DeBuhr, 2015) used for phase equilibria modelling with Theriak/ Domino (de Capitani & Petrakakis, 2010). Note that the composition is given in *mol* as required for Theriak/Domino modelling. The amounts of H, O and C were added to guarantee saturation with respect to graphite and a COH-fluid.

Si	Ti	Al	Fe^{2+}	Mn^{2+}	Mg	Ca	Na	K	H	C	O
50.34	0.60	31.21	5.55	0.06	4.00	0.15	2.59	5.50	100	50	212.49

(XR-μCT) scanner at Carleton University. The resolution of the scan was 12.08 μm using a X-ray energy spectrum of 40–130 keV, a beam current of 61 nA and an exposure time of 1300 ms for each 0.21° rotation step. Twenty scan frames were averaged to produce each single X-ray image. In order to remove low energy X-rays from the beam, a 0.25 mm brass filter was used to pre-harden the X-ray beam and to reduce the effects of beam hardening. A black and white flat field correction was applied before the scan to calibrate the detector signal in addition to black flat field corrections every 60 min during the scan. The X-ray attenuation data were converted into greyscale images that represent 12.08 μm thick slices by SkyScan NRecon software (Fig. 2).

Segmentation of XR-μCT Data

The scanned cylindrical core was reduced to a rectangular prism using Avizo software in order to remove beam hardening artifacts along the sample boundaries which could not be accounted for using low-energy X-ray filtering and conventional beam hardening correction algorithms. Biotite was automatically extracted from the CT data using Blob3D software (Ketcham, 2005) and a general greyscale range corresponding to the X-ray attenuation of this mineral. Chlorite grains with attenuation properties similar to those of biotite were discarded using Blob3D based on their contact relationships with cordierite. A primitive ellipsoid was fit onto each biotite crystal based on its surface area, providing the central positions, volumes, minimum, intermediate and maximum axis lengths as well as the aspect ratios and orientations of each crystal.

Cordierite porphyroblasts were extracted from the CT data through manual segmentation using Avizo. As the porphyroblasts consist of a range of X-ray attenuation, and therefore greyscale values that occasionally overlap with those of other minerals in this sample (Fig. 2), automatic segmentation, as done for biotite using a general greyscale range was not possible. Instead, an alternative method of segmentation was applied, in the following, referred to as the orthogonal slice method (Fig. 3). Regions of each cordierite porphyroblast were manually selected that correspond to perpendicular planes in the crystal that are approximately parallel to the minimum, intermediate and maximum crystal axes (Fig. 3a). The cordierite planes were then manually segmented based on the greyscale contrast between cordierite and its chlorite rim (Fig. 2). The extracted orthogonal slice objects were fit to a primitive ellipsoid using Blob3D so that the axis lengths could be obtained for the calculation of grain-specific parameters such as volume, central position, aspect ratio and orientation (Fig. 3b). To calculate the error introduced by the orthogonal slice method, a representative number of cordierite porphyroblasts was manually segmented to

compare their grain-specific parameters to the final ellipsoid that is fit onto the orthogonal slices (Fig. 3c, d). The volume obtained through full segmentation is larger than that obtained by the orthogonal slice method by $\sim$ 20–30%. However, the relative sizes between porphyroblasts remain the same and the positions of porphyroblast centres change by less than 6%. Changes to aspect ratio and grain orientation are negligible. It is important to note that the quantitative textural analysis performed in this study is based on the position of crystal centres and their relative sizes. For this reason, the orthogonal slice method applied here is considered an appropriate technique to segment a statistically relevant number of crystals that are characterized by relatively low attenuation contrast in XR-CT data sets, such as cordierite in metapelites from the Bugaboo contact aureole.

Statistical analysis of crystal distribution

A statistical analysis of the 3D distribution of cordierite and biotite crystal centres and relative sizes was conducted using Reduce3D software (version 3.27; Hirsch, 2000, 2011; Hirsch *et al.*, 2000). Reduce3D calculates scale-independent statistics across the entire sample volume as well as scale-dependent statistics to correlate texture with distance. By measuring multiple statistics, which consider different crystal features at varying distances, Reduce3D is able to uncover potential combinations of textures that together dictate the spatial distribution of porphyroblasts. The software requires information on each crystal centre (x–y–z coordinates) and an additional parameter, or mark, which typically relates to crystal size (e.g. radius, volume). This information was determined in this study through the segmentation procedures described above.

The statistics are compared to a null hypothesis envelope of 95% confidence that is created by simulating interface-controlled spherical crystal growth, defined by Kretz (1974), to create a crystal population of the same size distribution and crystal density as the sample volume in question. For these simulations, Reduce3D assumes a space-independent nucleation probability except for regions within pre-existing crystals. Furthermore, crystal centres are placed randomly with the largest final crystal sizes placed first as they are expected to have grown earliest under interface-controlled growth (Kretz, 1974; Hirsch, 2000; Hirsch *et al.*, 2000). When randomly placed crystals impinge upon another a test is run to see if the later placed crystal could have nucleated outside of the earlier placed crystal. This is done by subtracting the radius of the younger crystal from both crystals and checking whether the nucleation site of the younger crystal falls outside the boundary of the earlier crystal. On top of this placement criterion, two additional observability criteria are used to
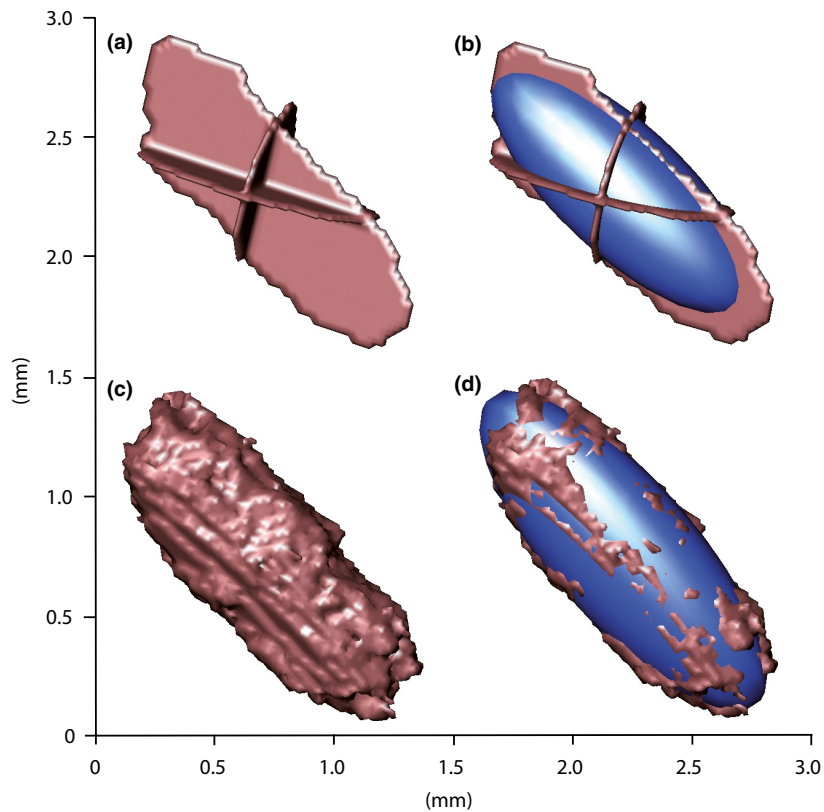
Fig. 3. Example of the orthogonal slice segmentation method used to quantify the texture of cordierite in this study. (a) Slices segmented using Avizo software are perpendicular to each other and are approximately parallel to the axes of the crystal. (b) An ellipsoid is fit onto the slices, and its minimum, maximum and intermediate axes are used to calculate the central position, aspect ratio, orientation and volume of the porphyroblast. (c) The same porphyroblast segmented fully in Avizo. (d) The ellipsoid fit onto the fully segmented porphyroblast is slightly larger than the ellipsoid in (b). However, the positions and relative sizes of cordierite porphyroblasts are approximately the same.

account for highly interpenetrated crystal pairs that, if present in the natural data, would be mistaken for a single crystal, while in the simulation they would be observed as two separate crystals. The observability criteria are explained in depth by Hirsch (2000) and Ketcham *et al.* (2005); analyses done here have used an observability filter with coefficient a1 = 0.85 and a2 = 3, as suggested by Hirsch (2000). The single-scale and correlation statistics are run on 100 simulated populations of interface-controlled crystallization to obtain results for a random distribution, and then the top and bottom 2.5% of the envelope are removed to achieve 95% confidence. In order to account for the modified sample volume formed during the segmentation process, a rectangular prism sample shape and the inscribed primitive option were used (see Hirsch, 2011).

RESULTS

Petrography

Sample COB3-S1-5 contains porphyroblasts of plagioclase, biotite, andalusite and cordierite in a fine-grained foliated matrix defined by white mica, ilmenite, quartz and chlorite (Fig. 4). Cordierite ranges in length from ~ 0.5–1.75 mm, is partly altered to fine-grained pinite and is surrounded by a ~ 100 μm thin rim of retrograde chlorite aligned parallel to S1 (Fig. 4a–c). Single chlorite inclusions are occasionally observed within the centre of cordierite without a specific orientation (Fig. 4b). Idioblastic andalusite ranges from 0.4 to 1.0 mm and occasionally displays diffuse chiastolite-like inclusion textures (Fig. 4c,d). Biotite ranges in size between 0.1 and 0.8 mm. Ovoid plagioclase porphyroblasts of 0.1–0.4 mm contain inclusion-rich cores relative to their rims but inclusion trails are not as prominent as in the other porphyroblasts. Inclusions of plagioclase, biotite and andalusite are observed in cordierite (Fig. 4c). Plagioclase and biotite inclusions in andalusite, and plagioclase inclusions in biotite are also present (Fig. 4d). These inclusion relationships suggest crystallization of plagioclase before that of biotite, and cordierite growth outlasting the crystallization of andalusite. Based on similar inclusion–matrix relationships, cordierite and andalusite appear to have started to crystallize concurrently.
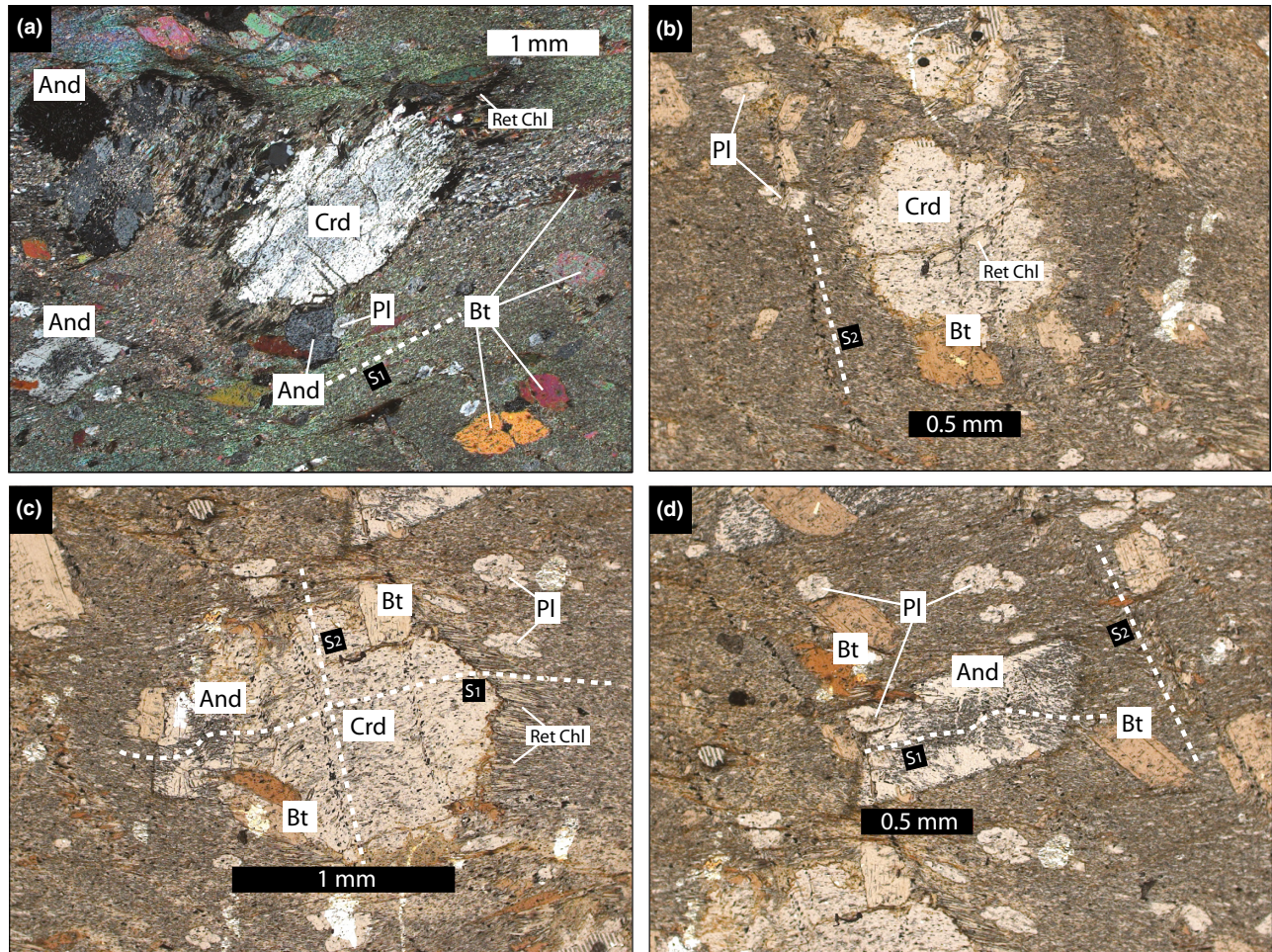
Fig. 4. Photomicrographs showing the textural relationships between plagioclase (Pl), biotite (Bt), andalusite (And) and cordierite (Crd). (a) Cyclic twinning in an elongated Crd with retrograde Chl (Ret Chl) along its rim. The elongation of Crd in this photo is parallel to the matrix foliation S1. Beneath Crd there are Pl and Bt inclusions within the rim of And. (b) Pinitized Crd with a Chl inclusion in its core and cross-cutting S2 Bt–ilmenite (Ilm) crenulations. (c) Inclusion relationships between porphyroblasts with And + Bt in Crd and a Ret Chl rim around Crd. (d) Chiastolite-like inclusion texture in And with merging inclusion trails and a Pl inclusion in And.

Fine-grained biotite and ilmenite define crenulations (S2) perpendicular to S1 that cut through porphyroblasts (Fig. 4b–d). These features are relevant to interpreting the position of porphyroblast centres should they have been repositioned from their original nucleation sites during late-stage deformation. The weak development of S2 and the observation that the crenulations are present within porphyroblasts instead of along their grain boundaries is a good indication that the deformation did not affect the position of the porphyroblasts.

Phase equilibria modelling

Phase equilibria modelling was applied to constrain the maximum P–T conditions of metamorphism experienced by COB3-S1-5. Phase equilibria modelling of representative metapelites of the entire Bugaboo aureole was discussed in detail by Pattison &

DeBuhr (2015) who found incongruities between observed and modelled phase equilibria for several different thermodynamic data sets and solid-solution models. One result that did not vary significantly, however, was the position of reaction (1) considered responsible for the mineral assemblage of COB3-S1-5. In order to test the relevance of the conclusions reached by Pattison & DeBuhr (2015) to our sample, calculated phase diagrams were calculated for the specific bulk rock composition of COB3-S1-5 (Table 1) using the same thermodynamic data sets as in Pattison & DeBuhr (2015). The results, in particular the position of reaction (1), are immaterially different from those calculated for the average metapelite composition of the aureole. The metamorphic pressure is constrained to ~3 kbar, based on the close coincidence of the incoming of K-feldspar and sillimanite, upgrade of andalusite development, in the aureole (Pattison & DeBuhr, 2015). For a pres-

sure of 3 kbar, the conditions for reaction (1) are ~ 550 °C, assuming a pure H_2O fluid. Assuming coexistence of the mineral assemblage with a COH-fluid in equilibrium with graphite, reaction (1) is displaced down-temperature by ~ 30 °C. In summary, our best estimate for the P–T conditions of metamorphism of COB3-S1-5 is 3 kbar and 520–550 °C.

Mineral chemistry

Individual cordierite grains are homogeneous with respect to their Na, Mn, Fe and Mg contents. There is also no significant variation in the abundance of these elements between different grains, which have an average Mg/(Mg + Fe) of 0.53. Biotite porphyroblasts are chemically homogeneous with Mg/(Mg + Fe) of ~ 0.41 matching the chemical composition of biotite inclusions present in andalusite and cordierite. The chemical compositions of homogeneous white mica and ilmenite do not vary as a function of their textural positions as matrix phases or mineral inclusions. Chlorite rims around cordierite are compositionally identical compared to chlorite grains present as mineral inclusions or matrix constituents. Albitic plagioclase is concentrically zoned, transitioning from an average Na/(Na + Ca) of 0.77 in the core to 0.93 in the rim. Representative EPMA results of matrix and porphyroblast phases of COB3-S1-5 can be found in Appendix S1.

Observed X-ray attenuation

A CT greyscale image is displayed in Fig. 5a alongside a thin section through the rock at the same location in Fig. 5b. Andalusite is outlined in the thin section and overlain on the tomography data, because its attenuation is similar to that of the rock matrix making it difficult to observe in the CT data. Biotite is the greatest attenuating porphyroblast phase, whereas cordierite displays an inhomogeneous distribution of X-ray attenuations within individual porphyroblasts. The greyscales within cordierite range from that of the matrix to black, with the black regions matching fractures seen in thin section (Fig. 5c,d,f). Cordierite is spatially related to retrograde chlorite, which is visible as a highly attenuating rim around each crystal. Porphyroblasts of plagioclase show a lower X-ray attenuation than the matrix (Fig. 5e) and are aligned parallel to S1 (Fig. 4). Biotite–ilmenite S2 crenulations are displayed through CT as fine highly attenuating linear features oriented at an angle to S1 and spaced evenly 0.5–1 mm apart (Fig. 5e); however, when cutting through cordierite porphyroblasts, S2 is not as visible in CT. (Fig. 5c,f).

Predicted X-ray attenuation

Calculations of the linear X-ray attenuation of phases occupying COB3-S1-5 are graphed in Fig. 6a against

X-ray energies up to 1 MeV. For these calculations, the observed mineral chemistries are used in combination with the mineral densities predicted by Theriak/Domino, and the NIST X-ray attenuation database (http://www.nist.gov/pml/data/xcom/index.cfm). Between 40 and 130 keV (Fig. 6b), the spectrum of X-ray energies for the scan performed in this study, ilmenite is the highest attenuating phase followed by biotite and chlorite, and the least attenuating phases (cordierite, andalusite, white mica, plagioclase and quartz) all have similar X-ray attenuation coefficients. Above 80 keV, however, the linear attenuation of andalusite, white mica and cordierite cross so that andalusite becomes a greater attenuating phase. The greatest intensity of X-rays for the scan performed is at ~ 100 keV, and the linear attenuation at this energy is the best representation of what the relative greyscale values of the phases will be (Fig. 6b).

Statistical analysis of the cordierite and biotite texture

The crystal volume distribution and volume to aspect ratio plots for the cordierite and biotite populations are displayed in Fig. 7. The aspect ratio of the biotite population ranges between ~ 1.5 and 9 for grains smaller than ~ 0.02 mm³ (Fig. 7c). The variation in aspect ratio reduces with an increase in volume and ranges between ~ 1.5 and 6.5 up to a volume of ~ 0.05 mm³, and approaches a range of ~ 2 to 4 for bigger grains. The crystal volume distribution of biotite is positively skewed (Fig. 7d). The major axes of the biotite best-fit ellipsoids are oriented in the plane 120/88, whereas the minor axes create a perpendicular lineation parallel to 08/012 (Fig. 8; orientations are given relative to the sample position during XR-μCT scanning and do not relate to a geographic system). Biotite is aligned parallel to S1 (Fig. 4), therefore, this planar structure formed by the major axis lengths is approximately parallel to the matrix foliation.

The aspect ratio of cordierite ranges between ~ 1.5 and 4.5 with an average of ~ 2.5 (Fig. 7a). There is no relationship between volume and aspect ratio, and the crystal volume distribution is unimodal and normal (Fig. 7b). The major axes of the cordierite best-fit ellipsoids lie in the plane 303/87, approximately parallel to the foliation of biotite and therefore S1. The minor axes create a planar feature at 014/86 perpendicular to S1 (Fig. 8).

Theoretical background of the statistical analyses

The single-scale statistics calculated by Reduce3D in this study include the ordering index, clustering index, impingement index and isolation index. The first two indices were introduced to 2D metamorphic texture analysis by Kretz (1966, 1969), whereas the impingement and isolation indices were contributed
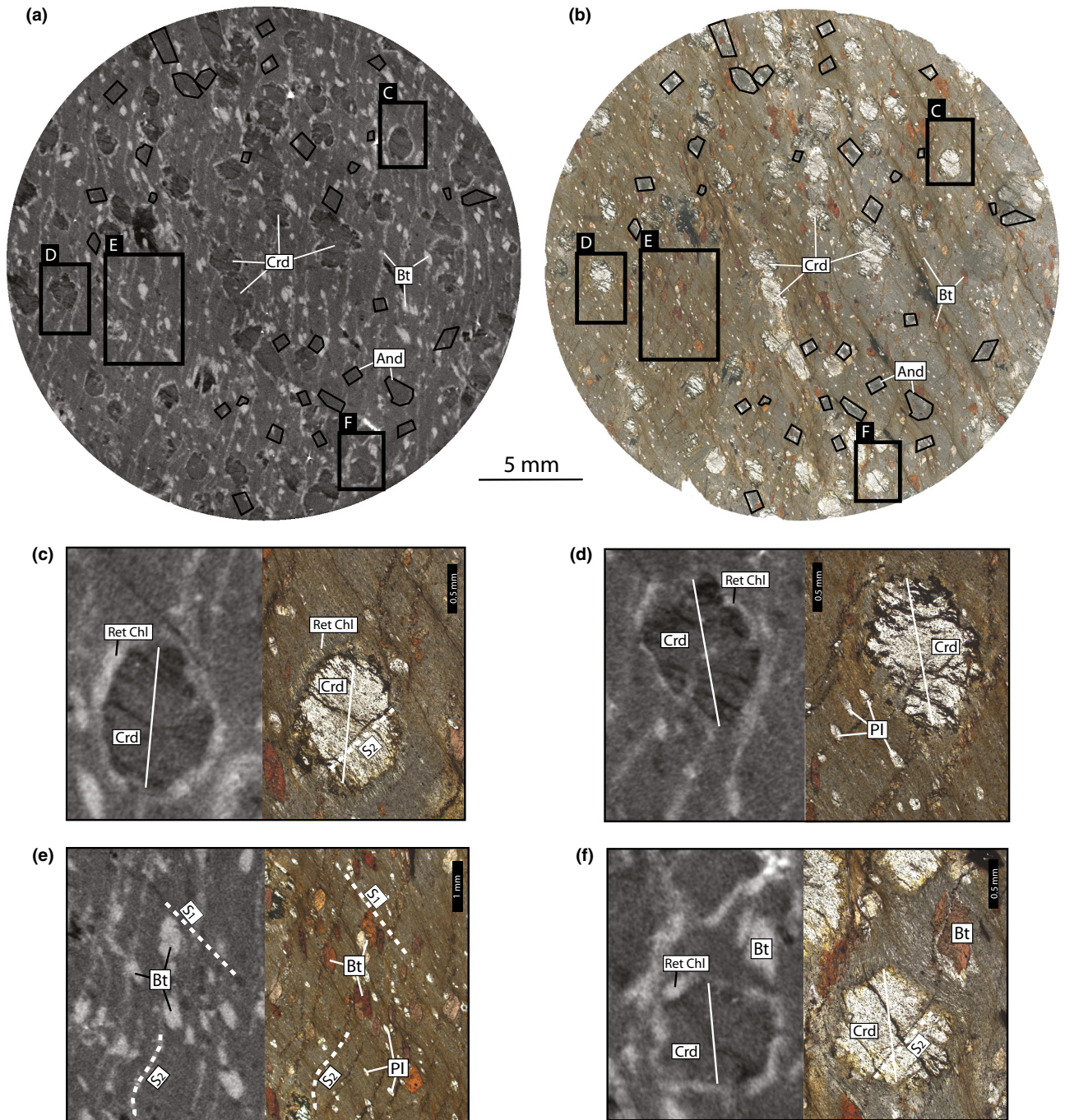
Fig. 5. XR-μCT greyscale image (a) with corresponding thin section photo (b). Greater linear X-ray attenuation coefficients are represented by greater greyscale values. Cordierite (Crd) and biotite (Bt) are visible whereas andalusite (And) cannot be distinguished from the matrix phases and is therefore outlined. Compositional traverses are done across Crd [unbroken lines in (c), (d) and (f)]. (e) The matrix foliation S1 represented by the alignment of plagioclase (Pl) and the S2 crenulation identified by highly attenuating Bt and ilmenite spaced at 0.5–1 mm.

by Carlson (1989) and extended to 3D by Hirsch (2000). Reduce3D (Hirsch, 2000, 2011; Hirsch *et al.*, 2000) is used to calculate and plot all of these indices in this research except for the isolation index which can be found in the output text file of this software (Appendix S2). The scale-dependent correlation functions calculated in this study are the L'-Function (L'F), the Pair Correlation Function (PCF) and the Mark Correlation Function (MCF'; Fig. 9). These functions, along with the single-scale statistics, have been used in 3D analysis of metamorphic rocks (e.g. Daniel & Spear, 1999) and were implemented into
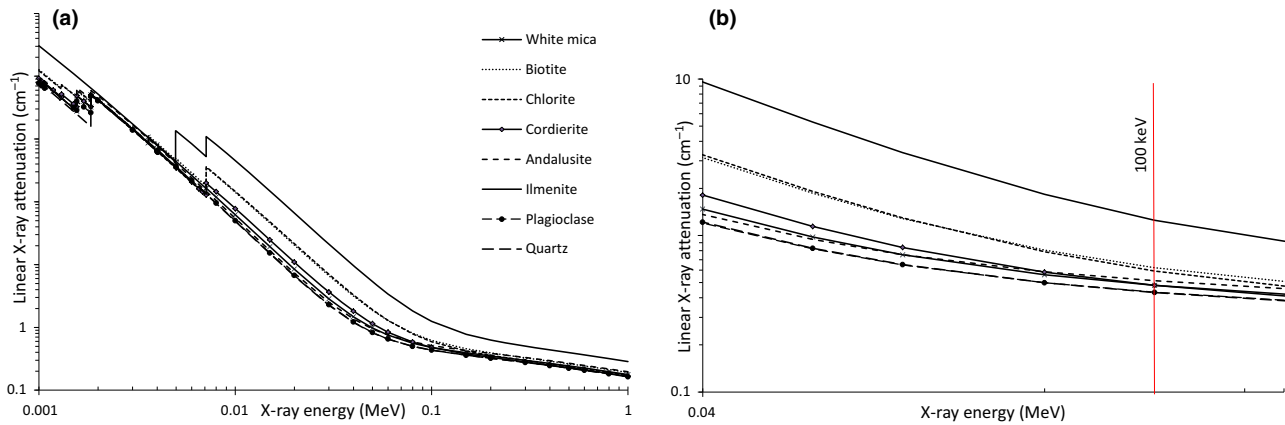
Fig. 6. The linear X-ray attenuation with incoherent scattering for the minerals in COB3-S1-5 for (a) an X-ray spectrum up to 1 MeV and (b) the X-ray spectrum of the CT scanner used in this study (40–130 keV). The greatest intensity of the X-ray spectrum is at ∼100 keV.

Reduce3D by Hirsch (2000). In general, the more sophisticated approaches inherent in the correlation functions are preferred to the single-scale measures as they allow for the quantification of textural relationships across a range of length scales instead of global averages (Carlson, 2011). In the following, the theoretical background of each statistic is briefly introduced before their applications to the sample investigated in this study are presented. Input files used with and output files generated by Reduce3D in this study are contained in Appendix S2.

Ordering Index. Also known as the aggregation index '*R*' and the nearest neighbour test (Clark &

Evans, 1954; Kretz, 1969; Carlson, 1989, 1991), the ordering index is the ratio between the average observed nearest neighbour distance in the sample and the average expected nearest neighbour distance in the random simulations (Clark & Evans, 1954; Kretz, 1966, 1969; Jerram *et al.*, 1996; Rudge *et al.*, 2008). When the observed nearest neighbour distance is greater than measured in the random simulation (*R*>1), the crystals are spaced farther apart and signify an ordered distribution. If the observed crystals are more closely spaced and the average nearest neighbour distance is less than what is expected (*R*<1), a clustered distribution is present. A random distribution gives a value *R*=1. The values given in
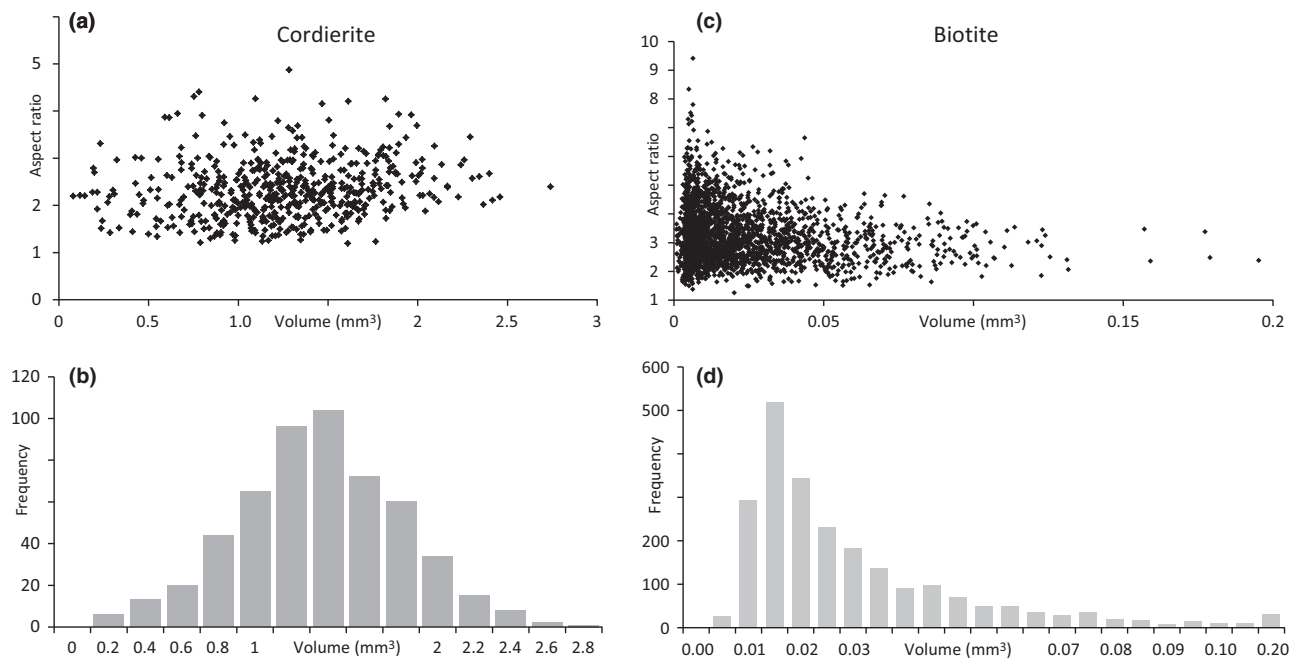

Fig. 7. Crystal volume–aspect ratio and crystal volume–frequency plots for cordierite (a, b) and biotite (c, d). The frequencies given correspond to the number of crystals per scanning volume.
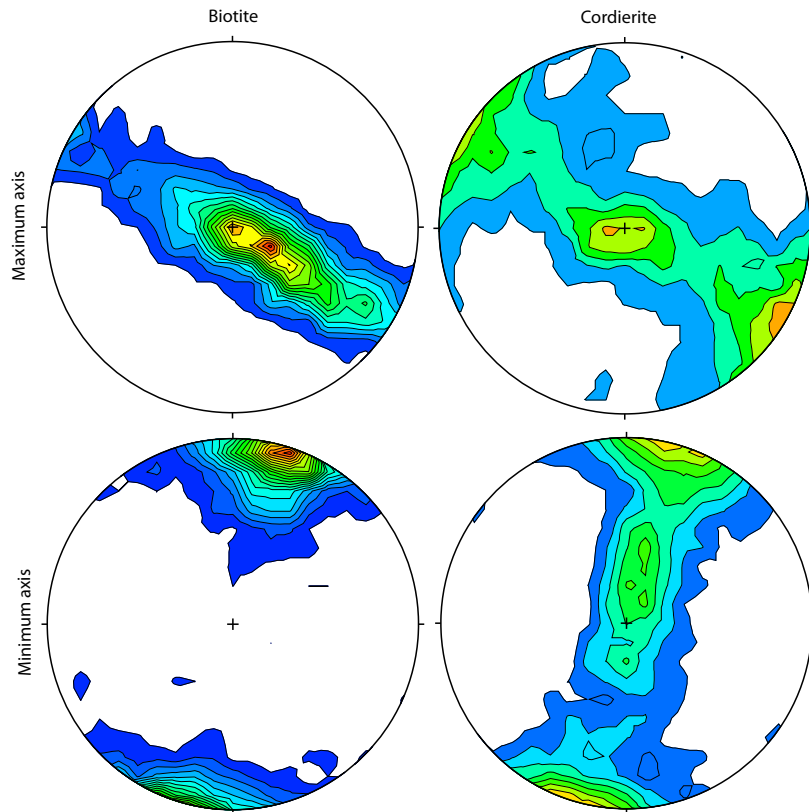
Fig. 8. Stereonet plots for the major and minor axes of the best-fit biotite and cordierite ellipsoids. The plots are relative to the orientation of the rock core during the XR-CT scan. The major axes of both biotite and cordierite lie within S1, and their minor axes are perpendicular to S1.

this study are equal to $1/R$ and compared to a 95% confidence envelope for a random distribution instead of unity. The null hypothesis is rejected if values fall outside the envelope in favour of either clustering or ordering depending on whether they fall above or below the envelope, respectively.

Clustering Index. First introduced as the random-point method for 2D analysis, the clustering index uses a random distribution of points and measures the distance from each of those points to the nearest crystal centre. The results for the natural sample are then compared to the results for a random distribution (Denison *et al.* 1997). A random array of crystals would result in a χ^2 distribution; however, to remain consistent, the value is divided by $2n$ to com-

pare to unity. A value <1 signifies an ordered distribution while a value >1 corresponds to clustering. This value is compared in our study to a 95% confidence envelope of interface-controlled crystal growth where values that fall above the envelope suggest clustering and below the envelope suggests ordering.

Impingement Index. The ordering and clustering indices only take into account the position of crystal centres, whereas the impingement index considers both position and size. Based on the Avrami ratio, this index compares the actual volume of crystals to an extended volume, which is the volume that would be obtained if the crystals grew without impingement (Carlson, 1989). The ratio is then tested against the same ratio for a random crystal array with the same
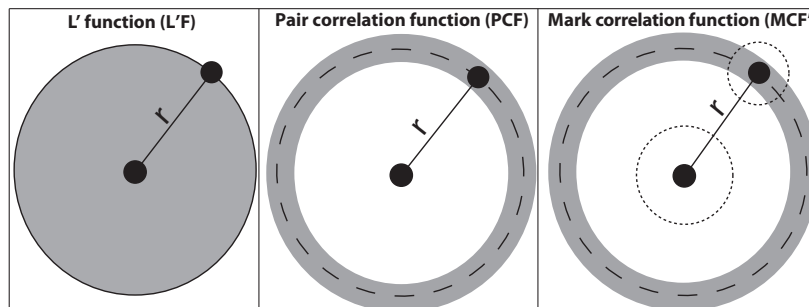

Fig. 9. Schematic of the scale-dependent statistics used in this study. L'F and PCF consider only the position of crystal centres whereas the MCF' takes into consideration the value of the input mark. See text for details.

crystal size distribution, which may contain a degree of impinging crystals if the placement and observability criteria are passed. If the actual and extended volumes are equal, then there is zero impingement within the crystal population, indicating an ideal ordered distribution. A random distribution would have an extended volume slightly larger than the actual volume, indicating a small degree of impingement whereas a clustered distribution, where many crystals may impinge on one another, would contain an extended volume much larger than the actual volume. This ratio is compared to a random distribution in order to consistently compare the value to the null hypothesis envelope as before. A value that falls above the envelope indicates clustering and a value below indicates ordering.

Isolation Index. The isolation index (D. Hirsch, pers. comm.) measures how much the average nearest neighbour crystal size deviates from the average crystal size. If the average nearest neighbour size is less than the average size of the entire crystal population, resulting in a positive value, then ordering is inferred. If the average nearest neighbour size is greater than the average size, creating a negative isolation index, then clustering of large crystal sizes may be present. This value can be found in the output text files of Appendix S2.

L′-Function. The L'-F originates from Ripley's 2D K-function (Ripley, 1976) which is a measure of the number of crystal centres that are present within a circular region around each crystal (Fig. 9). The K-function was transformed to the L-function to consider a spherical region for 3D analysis. The test sphere is defined by its radius, also known as the test distance (r), which increases with each test to account for the change in crystal abundance as the spherical volume grows. The L-function is normalized to obtain the L'-function in order to compare the final statistic to a random distribution and a value of zero. This is done around every crystal to achieve an average statistic for each test distance. If more crystal centres are present within a volume than found in the 100 simulated random arrays (positive statistic, above envelope), then clustering is present within that scale. If fewer crystal centres are present than found for a random distribution (negative statistic, below envelope), then an ordered distribution exists.

Pair Correlation Function. Similar to the L'-F, the PCF takes into account crystal centre positions, but instead of using a spherical test region, it uses a spherical shell (Fig. 9). This way, the crystal abundance at every test distance can be determined (instead of within every test volume). The shell is positioned at r and has a thickness that is determined by the bandwidth of an Epanecnikov kernel function (Hirsch, 2000). The idea of the kernel function is to allow all crystal centres within the shell to be considered. However, crystals closer to the centre of the shell (near the actual test distance) will be weighted more heavily than those that fall close to the edge of the shell. The thickness of the shell can be adjusted in Reduce3D by changing c ($c=0.1$ for all statistics done in this study). The PCF is normalized to a random distribution value of unity and compared to the position of the 95% confidence null hypothesis envelope. An abundance of crystals at a specific test distance will create a value above the envelope indicating clustering, while a scarcity of crystals will indicate ordering and result in a value below the envelope.

Mark Correlation Function. The MCF' is unique in that it takes into consideration an additional crystal feature, or mark, such as radius or volume. Similar to the PCF, the MCF' accounts for crystals present within a spherical shell around each crystal (Fig. 9). The arithmetic mean value of the mark for crystals separated by r is compared to the arithmetic mean mark value for the entire population. Accordingly, the MCF' does not measure deviations from random but variations in crystal marks. For example, if radius is used as the mark, and the mean radius of the crystals separated by r is smaller than the mean radius of the population, then an ordered texture is present. If the mean radius of the crystals in question is larger than the mean radius of the population, crystals spaced at this test distance are relatively large. The arithmetic mean is used for the MCF' instead of the geometric mean, because the latter has a tendency to reduce the statistic below unity (Hirsch, 2000). Accordingly, the results are visually compared to the same statistics for the random distribution simulations; no normalization is done making the MCF' a pure correlation between mark and scale.

Statistics for the cordierite and biotite pattern

The single scale and scale-dependent statistics for cordierite and biotite in COB3-S1-5 are shown in Fig. 10 using the sphere-normalized radii and the semi-major axes of the fitted ellipsoids as the mark (Table 2). The statistics are plotted against the test distance and compared to a 95% confidence envelope for a simulated random distribution (*blue* envelope).

With a sphere-normalized radius used as the mark, the ordering and clustering indices calculated for the cordierite population fall within the null hypothesis envelope of a random distribution whereas the impingement index falls below the envelope, possibly indicating that there is less impingement in the actual sample than for the random array (Fig. 10a). The L'F and PCF exhibit a random distribution at most scales, with values falling inside the 95% confidence envelope. However, at a length scale of ∼1 mm L'F and PCF calculations result in values below the 95% confidence envelope suggesting ordering of crystal sizes at that
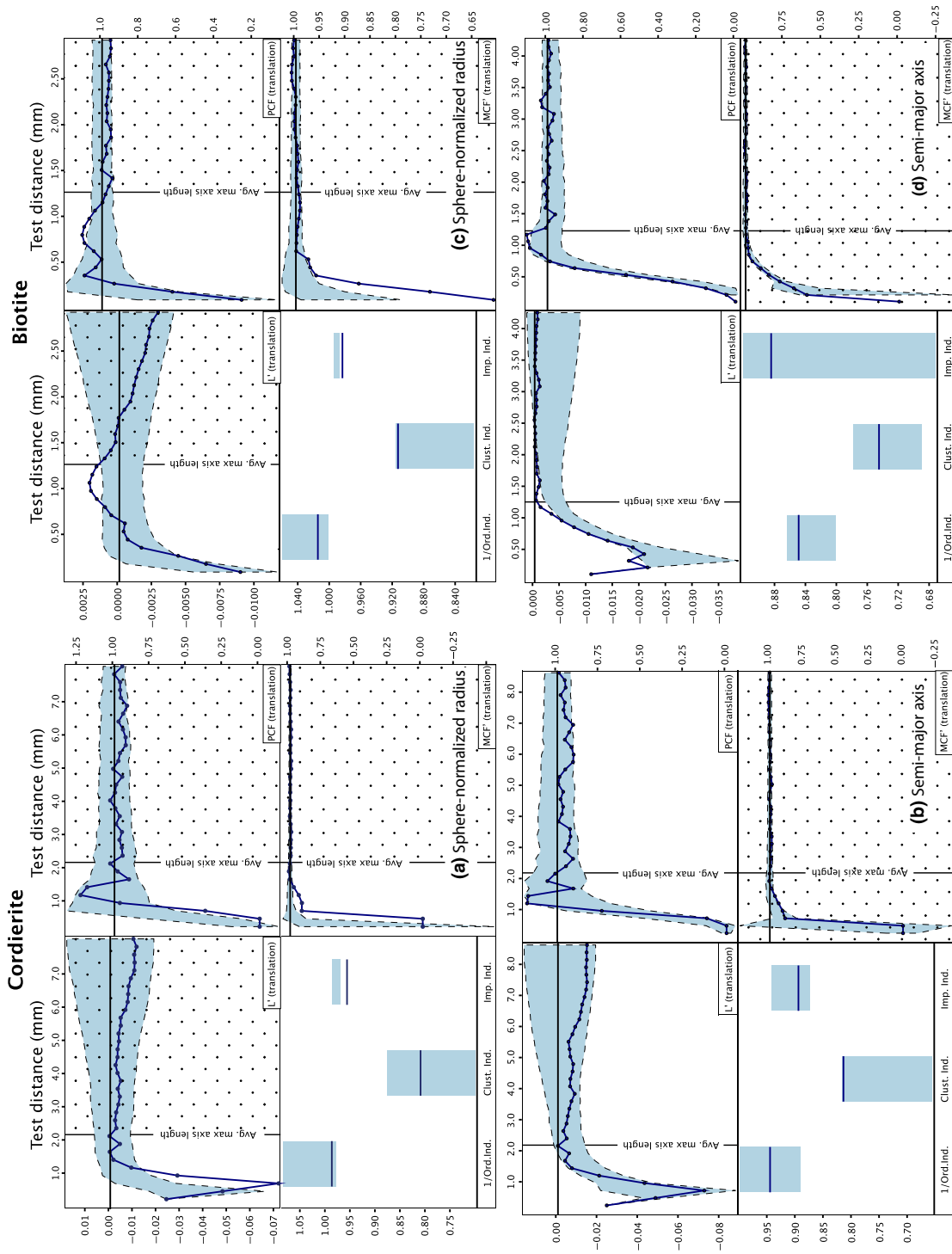
Fig. 10. Results of spatial statistical correlation functions and single-scale statistics calculated with Reduce3D (Hirsch, 2011) for cordierite and biotite using (a, c) sphere-normalized radius and (b, d) semi-major axis length of the best-fit ellipsoids as the marks. The *blue areas* correspond to theoretical results (with 2-σ envelope) obtained from non-clustered interface-controlled crystallization simulations obtained with Reduce3D according to a model developed by Hirsch *et al.* (2000). The *dotted* pattern indicates the length scales at which the corresponding correlation functions produce reliable results. See text for details.

Table 2. Lengths (mm) of sphere-normalized radii and semi-major axes of fitted ellipsoids (see Fig. 3) of the cordierite and biotite populations.

	Sphere-normalized radius	Ellipsoid semi-major axis
Cordierite		
Average (Min, Max)	0.65 (0.26, 0.86)	1.10 (0.41, 1.85)
Biotite		
Average (Min, Max)	0.16 (0.05, 0.35)	0.63 (0.27, 1.49)

same scale commonly expected to develop through diffusion-controlled nucleation and growth (e.g. Carlson, 1989, 1991, 2011). An almost perfect random distribution of crystal sizes is seen through the MCF' with the exception of scales at and below the average major axis length. Values for those scales plot below the envelope again possibly suggesting ordering as a result of diffusion-controlled nucleation and growth.

If the semi-major axes of the best-fit ellipsoids are used as the mark instead of sphere-normalized radii, a random crystal size distribution is obtained using L'F, PCF and MCF' for all scales across the rock volume studied (Fig. 10b). A random crystal size distribution is commonly interpreted to reflect interface-controlled reaction kinetics (e.g. Kretz, 1966, 1969; Carlson, 1989, 1991, 2011). Similar results are obtained when calculating the global ordering, clustering and impingement indices that all indicate a random crystal size distribution.

If the sphere-normalized radius is used as the mark in the statistics calculations of the biotite population (Fig. 10c), the ordering and clustering indices fall within the 95% confidence envelope whereas the impingement index falls below, an indication that there is less impingement than expected. The L'F and PCF display a clustering signal at length scales of ~ 0.75–1.25 and 0.75–1 mm, respectively, with all other scales falling within the null hypothesis envelope indicative of a random crystal size distribution. At length scales of less than ~ 0.5 mm, the statistical values fall below the envelope in the MCF' indicating an ordered texture for these length scales commonly inferred to reflect diffusion-controlled nucleation and growth.

If the semi-major axes of the best-fit ellipsoids of the biotite population are used as mark (Fig. 10d), then all three global indices indicate a random crystal size distribution in line with the predictions of the MCF'. The L'F and PCF also show a random distribution but at length scales of ~ 1.25 mm, where values are above the 95% confidence envelope indicating clustering at that same scale.

Both the scale-dependent and global statistics calculated for the cordierite and biotite populations strongly depend on the mark used in the calculations. If the semi-major axes of the best-fit ellipsoids are used, then a random disposition of crystal sizes is determined for both mineral populations using both the global and scale-dependent statistics (Fig. 10b,d).

This differs strongly from the ordered texture obtained at length scales shorter than the average major axis lengths of the mineral populations if sphere-normalized radius would be used as mark (Fig. 10a,c). This highlights the importance of the choice of that mark and, hence, the inherent geometrical model assumptions, for the interpretation of the statistics calculations.

INTERPRETATION AND DISCUSSION

X-ray attenuation

The predicted linear X-ray attenuations of minerals present in COB3-S1-5 (Fig. 6) match the relative grey-scale values obtained through CT scanning and data processing (Fig. 5a) with the exception of andalusite, which is predicted to have a higher attenuation than the matrix phases. This discrepancy may be explained by the abundance of fine low attenuating quartz inclusions that may reduce the overall attenuation of their andalusite host (Fig. 4d). The extraction of cordierite from COB3-S1-5 was favourable due to the contrast with their highly attenuating chlorite rims in addition to their heterogeneous X-ray attenuation. The variation in X-ray attenuation across cordierite is not a result of chemical heterogeneities (Appendix S1) but is instead interpreted to reflect the partial volume effect (e.g. Soret et al., 2007) due to local grain size reductions associated with grain fracturing. The comparison of the tomography and thin section data (Fig. 5) indicates that fracturing of cordierite grains may have caused the observed local variations in X-ray attenuation. Note that the linear attenuation calculated in Fig. 6 uses the density of cordierite predicted by Theriak/Domino based on its chemical composition, and that a reduction in grain density due to fracturing and the production of fine grained polycrystalline material in the fractures could not be considered in the calculations.

Figure 11 displays the linear attenuation of the Mg and Fe end-members of cordierite along with reductions in density from 2.64 g cm^{-3} to 2.0, 1.5 and 1.0 g cm^{-3}. A change in Mg–Fe content greatly impacts the attenuation of cordierite, as does a change in the density of cordierite, which together with the chlorite rims is interpreted to be the dominant reason for cordierite visibility through CT in COB3-S1-5. The fractures are not parallel to S2 and are not filled with alteration minerals (Figs 4 & 5), suggesting late-stage deformation that may be related to exhumation.

Extent of chemical equilibration

Cordierite and biotite are compositionally homogeneous across the entire rock volume with respect to the elements analysed (Appendix S1). This may reflect chemical equilibration with respect to these
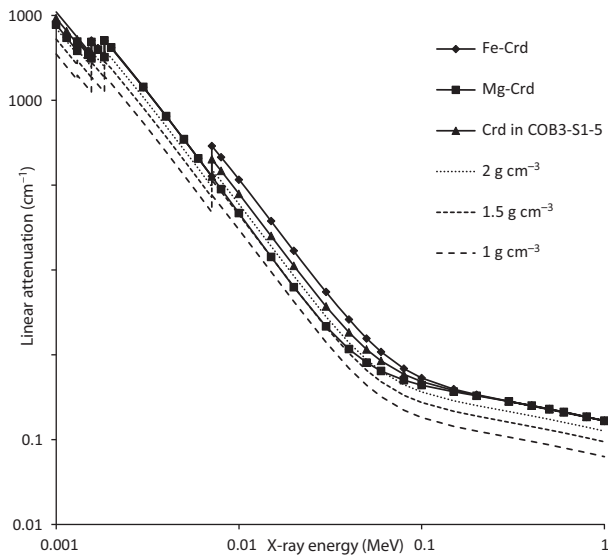
Fig. 11. The linear X-ray attenuation of the Fe and Mg end-members of cordierite compared to the observed chemical composition of cordierite in COB3-S1-5. A more Mg-rich cordierite will have a lower X-ray attenuation than one that is Fe-rich. A decrease in density also causes a decrease in X-ray attenuation and is a dominant reason for the visibility of cordierite in COB3-S1-5.

elements during or after porphyroblast crystallization. The identical $Mg/(Mg + Fe)$ of chlorite independent of its position in the rock may indicate whole-rock Mg–Fe equilibration after crystallization, most likely during retrograde metamorphism. However, the concentric Na–Ca zoning of plagioclase reflects chemical disequilibrium with respect to these elements possibly indicating relatively slow rates of intracrystalline diffusion of these elements in plagioclase and associated chemical fractionation at metamorphic conditions during its crystallization.

Crystal volume frequency distributions

In general, crystal volume distributions, similar to crystal size distributions, are the result of a complex interplay between various rock-forming processes such as nucleation and crystal growth. Resorption is an equally important process that potentially influences the size and shape distribution of crystals in rocks, and may substantially modify the primary nucleation and growth texture. The presence of a $\sim 100~\mu m$ thin retrograde chlorite rim around cordierite indicates that resorption occurred in this sample, consequently leading to reduced cordierite crystal sizes. However, this process is expected to not have significantly affected the spatial distribution of cordierite centres nor the relative extracted grain sizes.

The crystal volume distributions of cordierite and biotite obtained in this research are unimodal (Fig. 7) indicating that these crystals grew in a single metamorphic event. Furthermore, the unimodal distribu-

tions may be interpreted to reflect uninterrupted crystallization of these phases as repeated nucleation and growth may result in polymodal distributions instead. Unimodal crystal volume distributions similar to the ones observed may also form during repeated periods of crystallization if later nucleation events would be limited to the surfaces of previously grown crystals of that same phase. Repeated episodes of cordierite and biotite nucleation and growth on the surfaces of phases other than previously grown cordierite and biotite grains would result in polymodal crystal volume distributions which are not observed in the rock studied.

The crystal volume distribution of biotite is positively skewed, whereas the volume distribution of cordierite crystals is close to normal (Fig. 7b,e). This may be explained by a decrease in the number of energetically preferable nucleation sites that was more abrupt for biotite than for cordierite nucleation after a maximum nucleation rate was reached during progressive crystallization. Alternatively, a more sudden decrease in the availability of chemical nutrients required for biotite than for cordierite crystallization may explain the observed cordierite and biotite crystal volume distributions, and may be related to the demise of chlorite with increasing temperature.

Non-sphericity of crystals and the Strauss hard-core process

Previous statistical analyses of the distribution of porphyroblasts used sphere-normalized radius or volume as a mark for the calculation of global and scale-dependent statistics (Carlson, 1989; Daniel & Spear, 1999; Hirsch *et al.*, 2000; Ketcham *et al.*, 2005; Hirsch & Carlson, 2006; Hirsch, 2008). This may be reasonable when quantifying the distribution of crystals at length scales sufficiently larger than the average grain size of the crystal population. However, the Strauss hard-core process (Strauss, 1975; Ripley, 1981; Baddeley & Turner, 2000; Illian *et al.*, 2008; Rudge *et al.*, 2008) and its influence on rock texture cannot be correctly considered when sphere-normalized radius is used.

In general, the Strauss hard-core process results in an 'inhibitive' or 'ordered' pattern in a population of objects in 3D at length scales at which these objects touch each other. It is characterized by a positive correlation between the sizes of the objects and the distances between their centres as the centres of the objects can only get closer to each other if the sizes of the objects decrease. Accordingly, in a population of differently sized spheres, the Strauss hard-core process results in ordering at length scales less than the average diameter of the spheres. It is important to note that non-spherical objects such as crystals of any kind develop this pattern at distances equal to and less than the length of the average major axis of their best fit ellipsoids as those distances are the
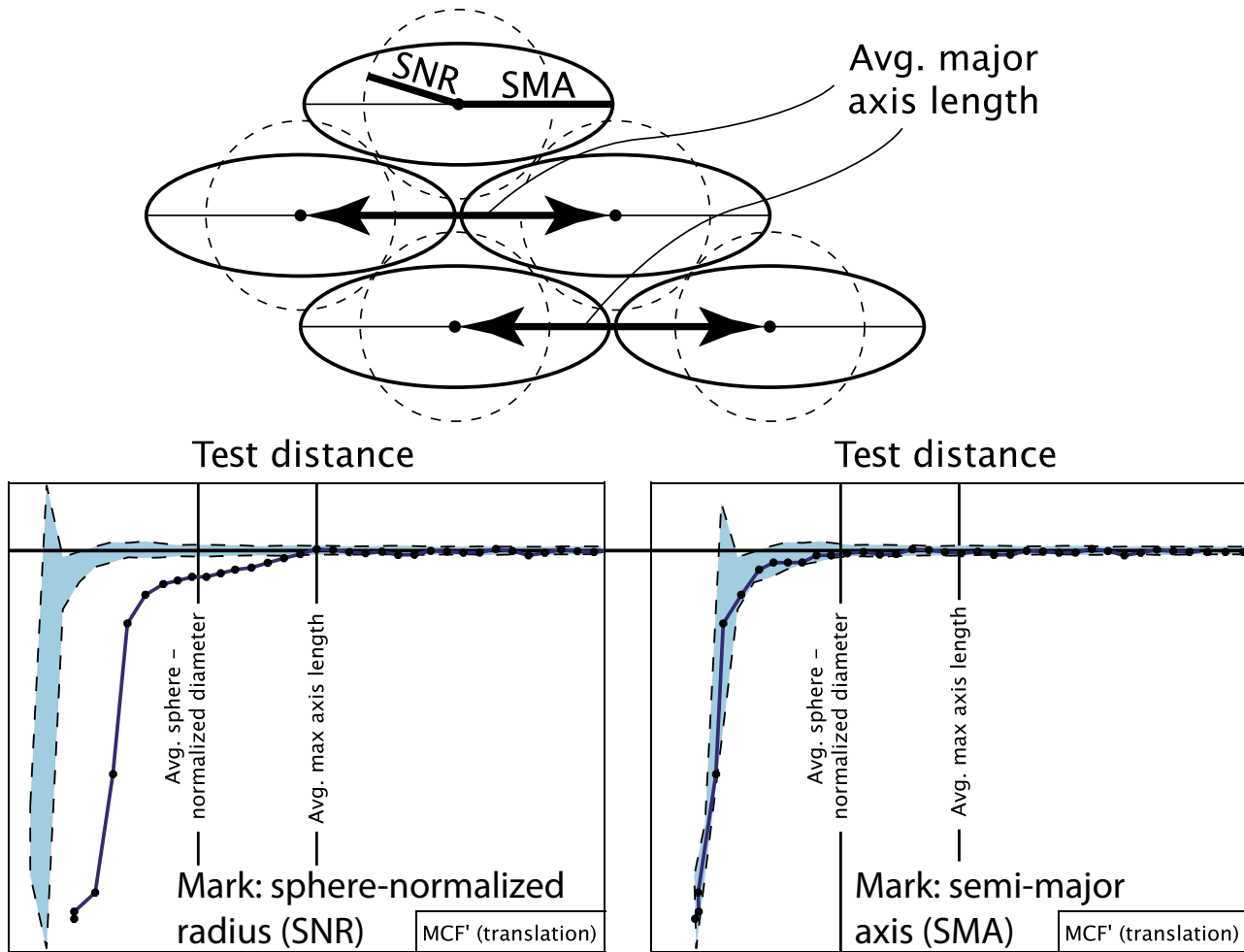
Fig. 12. Schematic showing that Strauss hard-core ordering of non-spherical objects develops at length scales equal to and less than the average major axis of the best-fit ellipsoid, i.e. at scales larger than the corresponding sphere-normalized diameter. SNR, sphere-normalized radius; SMA, semi-major axis.

length scales at which these objects touch. This phenomenon develops in any population of non-spherical objects independent of the orientation of the objects. More importantly, the length of the major axis of an ellipsoid fit around a non-spherical object exceeds that of the corresponding sphere-normalized diameter (Fig. 12). In other words, the Strauss hard-core process operates at length scales larger than the sphere-normalized diameter in a crystal population. Hence, there is a weakness in the correlation functions when applied to non-spherical objects (i.e. crystals) at length scales less than the average major axis if the sphere-normalized radius is used as mark in the statistics calculations. In such a case, the scale of ordering through the Strauss hard-core process would be underestimated and its characteristic ordered pattern may incorrectly be interpreted to be the result of diffusion-controlled nucleation and growth instead. However, using the semi-major axes as mark correctly accounts for the Strauss hard-core process and is principally useful when using the MCF'.

The semi-major axes should not be used as mark for L'F and PCF calculations as this would overestimate the crystal density of the sample volume relative to the simulated random array, potentially resulting in a false clustering signal. As the use of the sphere-normalized radius guarantees a correct representation of the sample crystal density, this mark may be used for the L'F, PCF and MCF' calculations but only above length scales at which the Strauss hard-core process operates. The length scales for which the correlation functions can reliably be used when applied to the cordierite and biotite populations in the sample studied are indicated using the *point pattern* in Fig. 10. Note that the Strauss hard-core process can only be accounted for when the MCF' is used together with the semi-major axis as mark. Underestimation of the Strauss hard-core process when sphere-normalized radius is used instead increases with the aspect ratio of the analysed crystals. For the aspect ratios of the cordierite and biotite populations studied here, Strauss hard-core ordering developed at

length scales of up to ~ 2.2 and 1.25 mm respectively. This is almost 1 mm longer than when sphere-normalized radius would have been used for both populations. It is therefore necessary to document the deviation from spherical geometry of the crystal population under investigation, and to account for its implications in the interpretation of statistical analyses.

CONCLUSIONS

The deviation of crystal shape from spherical geometry needs to be considered in the quantitative textural analysis of rocks. In this research, the geometry of cordierite and biotite crystals has been approximated by best-fit ellipsoids. Automatic segmentation of XR-CT data, as commonly done for minerals such as garnet or biotite, could not be used for the analysis of cordierite in this research because of too similar X-ray attenuation properties between cordierite and rock matrix phases. However, the semi-automatic orthogonal slice approach applied here is considered a useful alternative segmentation method. Weak pinnitization of cordierite rims and faint fracturing interpreted to have reduced the X-ray attenuation of cordierite crystals through the partial volume effect aid in the segmentation of CT data sets as it increases the X-ray attenuation contrast of cordierite relative to the rock matrix and has a negligible impact on the results of statistical texture investigations.

Using sphere-normalized radius for the calculation of L'F, PCF and MCF' as commonly done in the statistical analysis of crystal size distributions underestimates the length scales of ordering of crystals by the Strauss hard-core process and may result in unjustified inferences of diffusion-controlled nucleation and growth. In order to correctly account for the influence of the Strauss hard-core process on rock texture, the semi-major axes of the crystal population under investigation have to be used as mark in MCF' calculations. L'F and PCF do not account for the Strauss hard-core process in a population of non-spherical objects, and, hence, should only be used in the analysis of the spatial distribution of crystal sizes at length scales larger than the average major crystal axis.

The correct consideration of Strauss hard-core ordering in the scale-dependent statistical analyses conducted in this research indicates that both cordierite and biotite crystal centres and sizes are randomly distributed at any scale across the rock volume studied. The global ordering and clustering indices calculated for the rock sample also indicate a random distribution supporting the scale-dependent statistics for both mineral populations. Hence, the investigated textures corroborate interface-controlled nucleation and growth of cordierite and biotite associated with contact metamorphism in the Bugaboo aureole. Corresponding crystallization rates were likely dictated by attachment and detachment processes at the cordierite and biotite crystal surfaces and not by the rate of long-range diffusion across the rock matrix.

The ordered texture expected to develop during diffusion-controlled nucleation and growth would reflect competition for nutrients in the vicinity of growing porphyroblasts. The 3D random distributions of cordierite and biotite crystal centres as obtained through the calculations of the L' and PCF, and the random distribution of cordierite and biotite crystal sizes as indicated through the MCF' do not allow for such an interpretation. Furthermore, the observed chemical equilibration with respect to the major components of cordierite and biotite is additional evidence for relatively fast chemical transport rates between reactants and products of associated metamorphic reactions.

The drop in the abundance of relatively small crystals of the cordierite and biotite populations, which are assumed to have nucleated relatively late in the metamorphic history of the rock, is not related to an increased competition for nutrients. Instead, it may reflect a decrease in the number of energetically preferable nucleation sites, probably due to an increase in interfacial energies during progressive metamorphism, or the decrease in the nucleation driving forces associated with the demise of chlorite.

REFERENCES

Baddeley, A. & Turner, R., 2000. Practical maximum pseudo-likelihood for spatial point patterns. *Australian and New Zealand Journal of Statistics*, **42,** 283–322.

Brandon, A.D. & Lambert, R.S., 1992. Rb-Sr geochronology of Mesozoic granitoids in the southern Canadian Cordillera. Project Lithoprobe Southern Cordillera Transect, University of Calgary, Alberta, **24,** 95–104.

Carlson, W.D., 1989. The significance of intergranular diffusion to the mechanism and kinetics of porphyroblast crystallization. *Contributions to Mineralogy and Petrology*, **103,** 1–24.

Carlson, W.D., 1991. Competitive diffusion-controlled growth of porphyroblasts. *Mineralogical Magazine*, **55,** 317–330.

Carlson, W.D., 2011. Porphyroblast crystallization: linking processes, kinetics, and microstructures. *International Geology Review*, **53,** 406–445.

Chernoff, C.B. & Carlson, W.D., 1997. Disequilibrium for Ca during growth of pelitic garnet. *Journal of Metamorphic Geology*, **15**, 421–438.

Chernoff, C.B. & Carlson, W.D., 1999. Trace element zoning as a record of chemical disequilibrium during garnet growth. *Geology*, **27**, 555–558.

Clark, P.J. & Evans, F.C., 1954. Distance to nearest neighbour as a measure of spatial relationships in populations. *Ecology*, **35**, 445–452.

Connolly, J.A.D. & Cesare, B., 1993. C-O-H-S fluid composition and oxygen fugacity in graphitic metapelites. *Journal of Metamorphic Geology*, **11**, 368–378.

Daniel, C.G. & Spear, F.S., 1999. The clustered nucleation and growth processes of garnet in regional metamorphic rocks from north-west Connecticut, USA. *Journal of Metamorphic Geology*, **17**, 503–520.

de Capitani, C. & Petrakakis, K., 2010. The computation of equilibrium assemblage diagrams with Theriak/Domino software. *American Mineralogist*, **95**, 1006–1016.

DeBuhr, C.L., 1999. *Metamorphic Petrology and Mass Balance Analysis in the Bugaboo Contact Aureole*. PhD Dissertation, University of Calgary, Alberta.

Denison, C., Carlson, W.D. & Ketcham, R.A., 1997. Three-dimensional quantitative textural analysis of metamorphic rocks using high-resolution computed X-ray tomography: part I. Methods and techniques. *Journal of Metamorphic Geology*, **15**, 29–44.

Evans, K. & Powell, R., 2006. A method for activity calculations in saline and mixed solvent solutions at elevated temperature and pressure: a framework for geological phase equilibria calculations. *Geochimica et Cosmochimica Acta*, **70**, 5488–5506.

Evans, K.A., Powell, R. & Holland, T.J.B., 2010. Internally consistent data for sulphur-bearing phases and application to the construction of pseudosections for mafic greenschist facies rocks in Na_2O-CaO-K_2O-FeO-MgO-Al_2O_3-SiO_2-CO_2-O-S-H_2O. *Journal of Metamorphic Geology*, **28**, 667–687.

Fisher, G.W., 1978. Rate laws in metamorphism. *Geochimica et Cosmochimica Acta*, **42**, 1035–1050.

Gaidies, F., Pattison, D.R.M. & de Capitani, C., 2011. Toward a quantitative model of metamorphic nucleation and growth. *Contributions to Mineralogy and Petrology*, **162**, 975–993.

Gaidies, F., Petley-Ragan, A., Chakraborty, S., Dasgupta, S. & Jones, P., 2015. Constraining the conditions of Barrovian metamorphism in Sikkim, India: P-T-t paths of garnet crystallization in the Lesser Himalayan Belt. *Journal of Metamorphic Geology*, **33**, 23–44.

Hirsch, D.M., 2000. *Quantitative Studies of Porphyroblastic Textures*. PhD Dissertation, University of Texas at Austin.

Hirsch, D.M., 2008. Controls on porphyroblast size along a regional metamorphic field gradient. *Contributions to Mineralogy and Petrology*, **155**, 401–415.

Hirsch, D.M., 2011. Reduce3D: a tool for the three-dimensional spatial statistical analysis of crystals. *Geosphere*, **7**, 724–732.

Hirsch, D.M. & Carlson, W.D., 2006. Variations in rates of nucleation and growth of biotite porphyroblasts. *Journal of Metamorphic Geology*, **24**, 763–777.

Hirsch, D.M., Ketcham, R.A. & Carlson, W.D., 2000. An evaluation of spatial correlation functions in textural analysis of metamorphic rocks. *Geological Materials Research*, **2**, 1–42.

Illian, J., Penttinen, P., Stoyan, H. & Stoyan, D., 2008. *Statistical Analysis and Modelling of Spatial Point Patterns*. 1st Edition, Wiley-Interscience.

Jerram, D.A., Cheadle, M. J., Hunter, R.H. & Elliott, M.T., 1996. The spatial distribution of grains and crystals in rocks. *Contributions to Mineralogy and Petrology*, **125**, 60–74.

Ketcham, R.A., 2005. Computational methods for quantitative analysis of three-dimensional features in geological specimens. *Geosphere*, **1**, 32–41.

Ketcham, R.A. & Carlson, W.D., 2001. Acquisition, optimization and interpretation of X-ray computed tomographic imagery: applications to the geosciences. *Computers & Geosciences*, **27**, 381–400.

Ketcham, R.A., Meth, C.E., Hirsch, D.M. & Carlson, W.D., 2005. Improved methods for quantitative analysis of three-dimensional porphyroblastic textures. *Geosphere*, vol. **1** (no. 1), 42–59.

Kretz, R., 1966. Interpretation of the shape of mineral grains in metamorphic rocks. *Journal of Petrology*, **7**, 68–94.

Kretz, R., 1969. On the spatial distribution of crystals in rocks. *Lithos*, **2**, 39–66.

Kretz, R., 1974. Some models for the rate of crystallization of garnet in metamorphic rocks. *Lithos*, **7**, 123–131.

Kretz, R., 1983. Symbols for rock-forming minerals. *American Mineralogist*, **68**, 277–279.

Müller, T., Baumgartner, L.P., Foster, C.T. & Bowman, J.R., 2009. Crystal size distribution of periclase in contact metamorphic dolomite marbles from the Southern Adamello Massif, Italy. *Journal of Petrology*, **50**, 451–465.

Pattison, D.R.M. & DeBuhr, C.L., 2015. Petrology of metapelites in the Bugaboo aureole, British Columbia, Canada. *Journal of Metamorphic Geology*, **33**, 437–462.

Ripley, B.D., 1976. The second-order analysis of stationary point processes. *Journal of Applied Probability*, **13**, 255–266.

Ripley, B.D., 1981. *Spatial Statistics*. Wiley, New York, NY.

Robyr, M., Carlson, W.D., Passchier, C.W. & Vonlanthen, P., 2009. Microstructural, chemical and textural records during growth of snowball garnet. *Journal of Metamorphic Geology*, **27**, 423–437.

Rudge, J.F., Holness, M.B. & Smith, G.C., 2008. Quantitative textural analysis of packings of elongate crystals. *Contributions to Mineralogy and Petrology*, **156**, 413–429.

Sayab, M., Suuronen, J.-P., Hölttä, P., Aerden, D., Lahtinen R. & Kallonen, A.P., 2015. High-resolution X-ray computed microtomography: a holistic approach to metamorphic fabric analyses. *Geology*, **43**, 55–58.

Soret, M., Bacharach, S.L. & Buvat, I., 2007. Partial-volume effect in PET tumor imaging. *The Journal of Nuclear Medicine*, **48**, 932–945.

Spear, F.S., 1993. *Metamorphic Phase Equilibria and Pressure-Temperature-Time Paths*. Mineralogical Society of America Monograph. Mineralogical Society of America, Washington, DC.

Strauss, D.J., 1975. A model for clustering. *Biometrika*, **62**, 467–475.

SUPPORTING INFORMATION

Additional Supporting Information may be found in the online version of this article at the publisher's web site:

Appendix S1. Chemical analyses of cordierite, biotite, plagioclase, white mica, and ilmenite in COB3-S1-5.

Appendix S2. Input files used and output files generated by Reduce3D (Hirsch, 2011).